



New methodologies for on-site characterization of line-focus solar collectors' fields

Final report on autonomous robot and UAV with remote sensing capability for large solar fields

| | |
|--|--|
| STAGE-STE Project | |
| Scientific and Technological Alliance for Guaranteeing the European Excellence in Concentrating Solar Thermal Energy | |
| Grant number: | agreement 609837 |
| Start date of project: | 01/02/2014 |
| Duration of project: | 48 months |
| WP11 – Task11.2.2 | D11.8 |
| Due date: | January/2018 |
| Submitted | |
| File name: | WP11 D11.8 - Final report on autonomous robots and UAV with remote sensing capability for large solar fields |
| Partner responsible | ENEA |
| Person responsible | Marco Montecchi |
| Author(s): | Marco Montecchi (ENEA), Peter King (Cranfield), Eneko Setien Solas (CIEMAT), Raphael Albert (CEA) |
| Dissemination Level | PU |

List of content

| | | |
|---|---|----|
| 1 | Introduction..... | 4 |
| 2 | Geometrical measurements by close-range photogrammetry..... | 4 |
| 3 | Vacuum status of linear receivers..... | 10 |
| 4 | Check of mutual optical alignment receiver-reflector for parabolic-trough and linear-Fresnel modules..... | 15 |
| 5 | Flux measurement system..... | 25 |
| 6 | Conclusions..... | 29 |

Executive Summary

This deliverable, D 11.8 – Final report on autonomous robots and UAV with remote sensing capability for large solar fields, is part of the *WP11 Linear focusing STE activities* contained within *task 11.2. New methodologies for dynamic testing and predictive maintenance of large solar fields*, and *subtask 11.2.2 New methodologies for on-site characterization of line-focus solar collectors' fields*.

This final report summarises the results of three different techniques that appear very promising for the accomplishment of fast checks across large line-focus solar fields when embarked on UAVs, being this one of the purposes of the ongoing project STAGE-STE project. Although the activities done during the project life brought to important progress for all the considered techniques, in the end the *autonomous* flight management remains underachieved, matter of future work. Therefore the content of the present document does not completely fit the title which was set at the beginning by someone of the project designers. In our defence we would highlight the objective difficulty of developing any new airborne technique even just for the complexity of the flight management itself.

The report also includes a fourth technique concerning the measurement of the flux distribution in the focal region of a Fresnel solar plant. The measurement is done thanks to several CPV cells fixed on a transversal bar located below the receiver. The bar is able to move along the receiver to acquire an entire flux map. The measurement could be easily automatized allowing the flux mapping of the whole solar plant, for example by an autonomous robot.

1 Introduction

The increasing number of commercial solar thermal power plants is demanding the definition of predictive maintenance procedures to improve reliability and the number of operating hours. The most important inspections on solar fields are:

1. Optical and thermal analysis of linear solar receivers on-site;
2. Optical and geometrical analysis of line-focus reflectors on-site;
3. Status testing of the heat transfer fluid;
4. Testing of other components.

The integration of remote sensors in both terrestrial and aerial vehicles for fast characterization of line-focus solar fields is one of the purposes of the ongoing project STAGE-STE. This document summarises the results obtained with the accurate study of three different techniques which appear quite promising to accomplish fast checks across large line-focus solar fields by means of UAVs.

Concerning ground robots, the most skilled partner (Tekniker) could not continue the activity after the publication of the MS41 because of insufficient internal resources.

2 Geometrical measurements by close-range photogrammetry

Close-range photogrammetry is one of the most diffuse techniques used in CSP for the geometrical characterisation of structures and components. The main components are a high resolution camera and a set of targets. The technique requires that a pattern of targets are placed on the important areas of the object. Targets should be high contrast black and white, or retro reflective. This improves both the point recognition and the accuracy of the algorithms used to find the central points of each target. The targets may be constructed of a coded ring or sequence of shapes surrounding a central disk. These coded rings enable automation of the photogrammetry point matching. The target placement is currently manual, requiring direct access to all the required points and may take significant time depending on the required coverage. Ideally targets should be easily applied and detached, leaving no adhesive residue and may be presented as sheets to lessen the application time. Following the target application, several photographs must be taken, from different angles, using a high quality, low distortion camera. This is typically a DSLR camera with high resolution, large sensor and a fixed focus lens. The photographs should be taken from different points of view surrounding the object, covering as many angles as are practical. The camera and lens system must be calibrated to reduce the distortion of the images. This may be done away from the object, by using calibration sheets, or alternatively may be done using the actual photographs taken of the object. This method is preferred, as it replicates the exact lens settings and object that is under measurement. To aid in this calibration the camera should be rolled around the optical axis for some of the photographs. The lens parameters obtained are then considered in the image processing. Most photogrammetry software allows the use of automatic target matching utilising the coded targets, but some point selection and corrects may be required. It is possible to fully automate the image analysis and processing. A scale must be introduced into the model, which may be formed from a known scale bar introduced into the

photographs, with photogrammetry targets attached.

Advantages of the technique are low cost, and high accuracy (typically some mm for objects sizing tens of metres and less than 0.1mm for facet sized objects). Disadvantages are the need to apply targets to the surfaces, the semi-manual image processing, and the low spatial density of the measured points.

Photogrammetry can be used to measure the collector geometry. Because collectors are not perfectly rigid, their shape is generally affected by the gravity, depending on their orientation. Therefore aerial photogrammetry is a very important tool because allows the collector geometry to be determined in working orientations along its daily trajectory.

Cranfield University has previously developed a photogrammetry technique for measuring a range of solar collectors, including parabolic trough facets and modules. This technique has been validated to better than 100 microns against a tactile coordinate measuring machine, itself traceably accurate to less than 10 microns over the size of a typical facet. The photogrammetry technique involved a handheld camera, and has now been extended to operate with a UAV mounted camera. Handheld photogrammetry measurements have been performed on EuroTrough collectors, both at the individual facet and whole module scales. When measuring whole modules it is necessary to use larger diameter photogrammetry targets, due to the increased distance required from the mirror and the wider field-of-view.

Measurements at CIEMAT-PSA of whole modules used 9 targets per facet each with a central disk size of 30 mm. Using only 9 targets decreases the time required to attach and remove the targets and so is more suitable than covering whole facets when investigating a number of modules.

There is a general requirement for photogrammetry that the target should have an on-sensor size of greater than 5 to 10 pixels for proper identification. The 30 mm target size is sufficient for correct identification of both the central disk and the surrounding coded target ring at a distance of up to 15 m between camera and target, at angles up to 45 degrees. For capturing more than one trough, it may be necessary to use larger targets; however this could be calculated as required by using the field of view and resolution of the camera with the size of the required area for capture. In the case of the EuroTrough measurements, 9 targets were sufficient to identify millimetre scale errors both in module shape and facet alignment.

2.1 Experimental comparison of different types of UAV

The Cranfield UAV has been defined through consultation and testing with the UK company HexCam, which operates and provides training for multi-rotor drones, including capturing images and videos.

The initial set of experimental drone measurements were performed with two different drones and camera set ups. The first a commercial DJI Inspire quadcopter with built in stabilised 12 Mpixel camera with 1/2.3 inch sensor and fixed optics (Fig. 1), the second a custom built hexacopter with a gimbal mounted Sony NEX-7 24 Mpixel camera with an APS-C size sensor and fixed zoom lens (Fig. 2).



Fig. 1. DJI Inspire UAV



Fig. 2. HexCam hexacopter

Both set ups were used to measure two 1.6 x 1.2 m facets in different orientations, with both large and small photogrammetry targets as shown in Fig. 3.

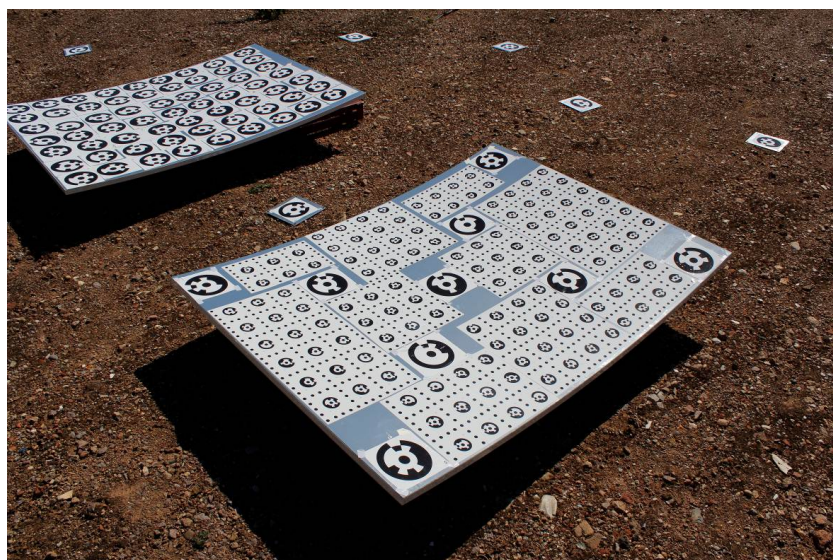


Fig. 3. Photogrammetry mirror set up

It was found that the larger sensor and higher quality optics of the NEX-7 camera produced significantly higher quality images and thus a more reliable and more accurate photogrammetry measurements than could be obtained using the small sensor built-in camera of the DJI Inspire (Fig. 4).



Fig. 4. Close-up of photogrammetry targets with NEX-7 (left) and DJI Inspire (right)

These results indicated that DSLR-type large sensor cameras are preferred to the built-in cameras available with some commercially available drones.

2.2 Experimental comparison of ground and UAV based photogrammetry

To evaluate the effect of moving to a UAV mounted camera on the size of the targets required, a vertical distance test was performed where photographs were taken from different heights looking straight down at the targets on the mirrors. This was investigating only how the distance away affects the target recognition not the accuracy of the system. Mirrors had a mixture of large (30mm centres) and small (10mm centres) targets. At 5m the field of view did not cover all of the large targets, so presents a smaller total number of targets. The results are shown in Table 1.

| Height (m) | Small targets (10mm) | Large targets (30mm) |
|------------|----------------------|----------------------|
| 5 | 126/126 | 78/78 |
| 10 | 2/126 | 83/83 |
| 15 | 0/126 | 83/83 |
| 20 | 0/126 | 70/83 |
| 25 | 0/126 | 10/83 |
| 30 | 0/126 | 4/83 |

Table 1. Number of targets correctly identified at different heights

It can clearly be seen that the smallest high density targets cannot be used at any increased distance, whereas the larger targets can be used up to around 15m without any targets being missed. This distance would be sufficient to capture at least a single trough module of 12m in length. Larger targets can also be used if larger areas require surveying in a single photograph.

Ground based photogrammetry was then performed using both the Canon and NEX-7 to compare the quality of the output against the DSLR previously verified.

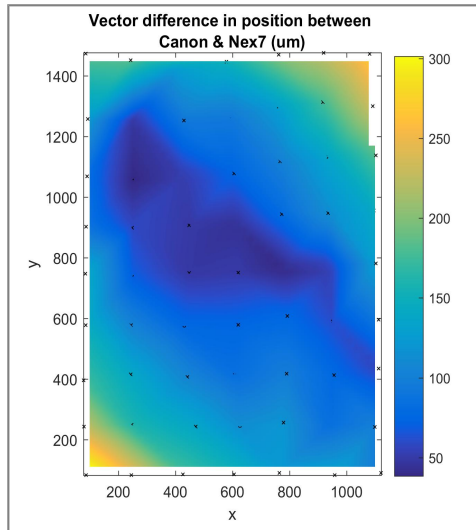


Fig. 5. Difference between Canon 600d and Nex7- both handheld

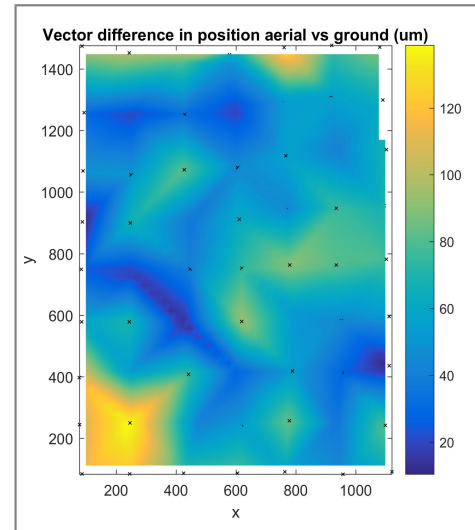


Fig. 6. Difference between Canon 600d and aerial Nex7

Fig. 5 shows the difference between two sets of points, one generated by handheld measurements using the Canon 600d and the other with handheld measurements using the Sony NEX-7. There is an RMS difference over all the points of 135 microns and a maximum deviation of 300 microns. Fig. 6 shows the difference between two further sets of points, the first generated by handheld measurements using the Canon 600d and the second with aerial measurements using the Sony NEX-7. There is an RMS difference over all the points of 69 microns and a maximum deviation of 140 microns. These initial results imply that measurements made on the ground, with different cameras, and with aerial cameras produce similar surface maps.

A forced displacement of 0.75mm was introduced to the middle support points to distort the mirror, and measurements were done to try to see the effect of this displacement. The results shown in Fig. 7 demonstrate the good agreement (to within 0.05mm RMS) between measurements done on ground and in the air.

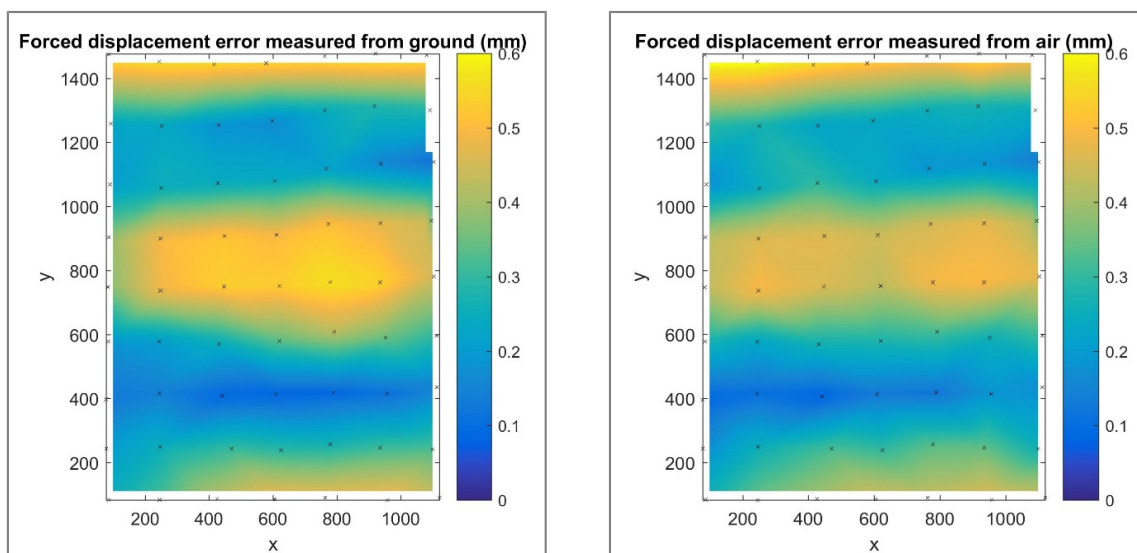


Fig. 7. Forced displacement comparison



Fig. 8. Westmill wind and solar park

Flights were carried out at Westmill wind and solar park, which included testing the navigation systems of the UAV over the site and also incorporated a larger target area than the previous tests, shown in Fig. 8. This enabled a more representative area to be measured, at a more appropriate distance from the targets. The same mirrors were used as for the previous tests and photogrammetry was performed both from the ground and from the air. The resulting surface maps were compared to one another and the results in Fig. 9 showed the good agreement of ground and UAV measurements as found previously, with differences of less than 0.7mm.

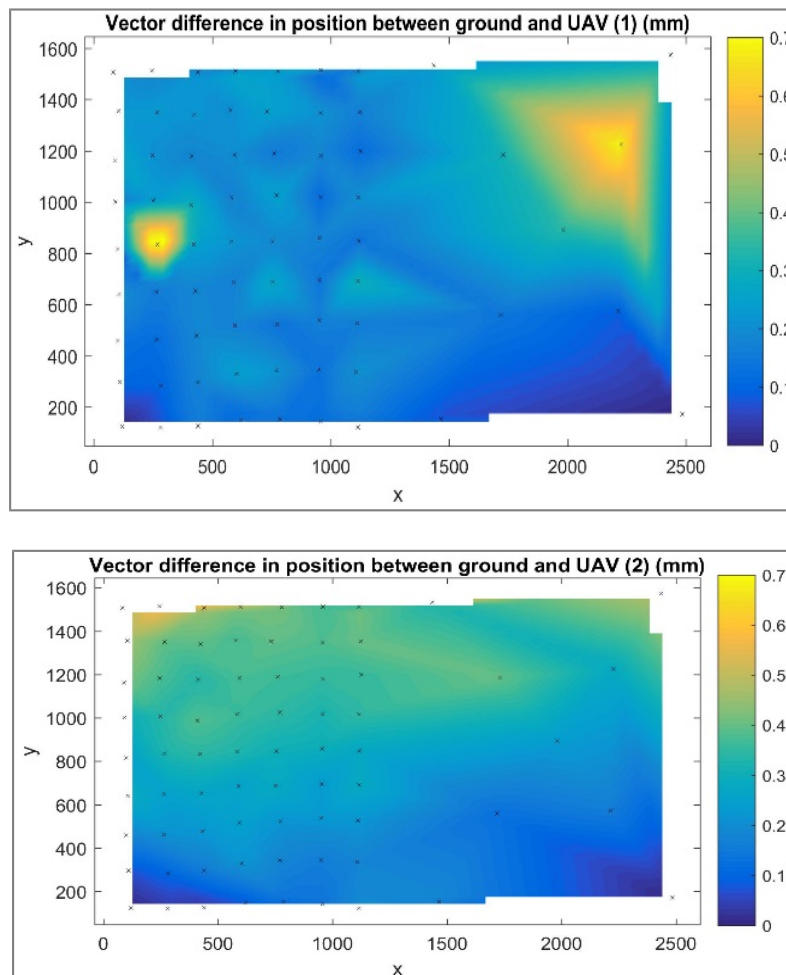


Fig. 9. Comparison between ground and UAV surface maps

This was despite poor weather during the testing with significant cloud cover with gusting winds and some rain halting the tests. Such weather issues will have a higher impact on photogrammetry when performed from the air compared to the ground. To some extent poor lighting can be easily seen and adjusted when the camera is being held for ground photogrammetry, but this is harder to account for during the UAV flights. Limited battery life means that repeatedly landing to make small adjustments to camera settings is not practical and can take a long time. Wind also can have a major effect on the UAV, causing unwanted movement. Although the UAV has built in GPS and position and orientation holding capabilities, these are limited by the response time of the system. For low speed constant winds the UAV can hold steady to an acceptable level, however it is the gusting winds which will cause sudden movements. These movements can cause motion blurring of the photographs, when it cannot be compensated by the UAV and gimbal set up.

2.3 Conclusions

In general there are a number of factors that affect the performance of photogrammetry when moving from the ground based system to a UAV based system. It has been found that the cameras on most commercially packaged UAV systems, such as the DJI Inspire, are not of sufficient quality for accurate photogrammetry. Larger DSLR type cameras are still required and so larger UAVs should be used which can accommodate these cameras. Under ideal weather conditions there is minimal loss of photogrammetry performance by using a UAV system, as long as the appropriate stabilisation and gimbals are used. However, UAV systems are more sensitive to weather conditions, particularly wind and will not be operative once the wind is sufficiently high or of a gusty nature. There are also many regulatory barriers to using UAVs, which vary from country to country. Such regulations are being continually developed in light of the development and growing number of UAVs.

3 Vacuum status of linear receivers

The thermal insulation of the evacuated receiver strongly depends on the vacuum state; when lost, the outer temperature increase and part of the absorbed solar energy is dissipated by thermal convection and radiation, reducing the receiver effectiveness. Because large parabolic trough solar fields consist of tens of thousands of receiver tubes, a fast non-contact method for checking the receiver vacuum state is highly desirable.

In this sense, one method of interest is the so called, **surface temperature method**. This method relates the temperature of the inner tube and the glass envelope with the vacuum state. The temperature of the glass surface is measured with an Infrared (IR) camera which is a non-contact measurement. As it is shown in Fig. 10, the radiation from the tube reaches the IR camera through the atmosphere. The signal is converted to value of superficial temperature of the glass tube assuming a value of the glass emittance ϵ .

The temperature of the inner tube can be determined with 2 different approaches: a) considering the temperature of the metal equal to the average temperature of the HTF, and b) by means of non-contact methods like thermographic cameras or pyrometers.

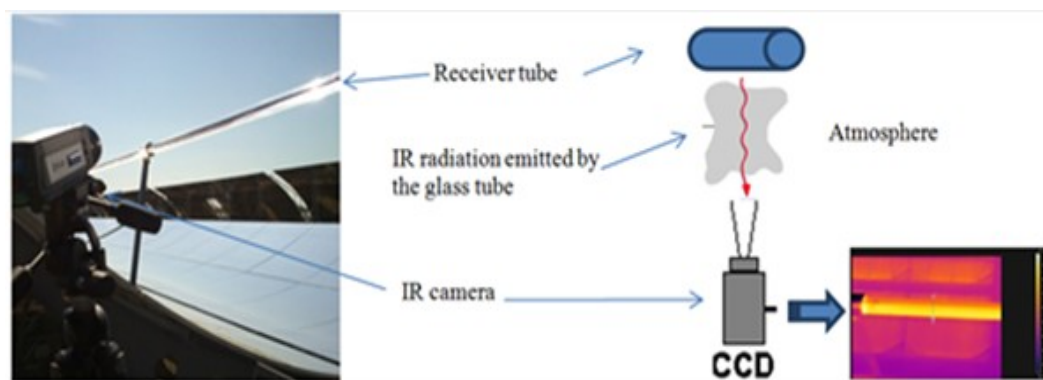


Fig. 10. Scheme of surface temperature method.

The surface temperature method has been widely used in the solar thermal plants, where a terrestrial vehicle or the operator itself move the camera along the solar field to localize the PTC receivers without vacuum. However, this method is very time-consuming due to the large size of solar fields, and it doesn't allow localization of the tubes with partially lost vacuum.

Within the framework of the STAGE-STE project, two major improvements of this technique have been proposed. The first improvement is the extension of this method to estimate the partial vacuum loss of PTC, and the results are shown in deliverable 11.7. The second improvement is based on the use of a UAV to carry the IR camera. This will allow faster and more automatic large solar field inspections.

In this work, the convenience of using a UAV to bring the IR camera during the vacuum status inspection of PTC receivers in large solar fields is explored.

3.1 Methodology

The potential of using a UAV to measure the PTC receiver's glass temperature from the sky has been tested in the HTF test loop facility at the PSA under solar real operation conditions. Two identical tubes, one of them with vacuum and the other one with no vacuum (10^{-4} mbar and 10^3 mbar), have been selected and characterized. The characterization of the tube receivers includes the measurement of the glass at different absorber temperatures (100, 200, 250, 300 and 350°C). The measurements of the glass have been carried out from the sky as a UAV would. Additionally, this characterization has been replicated in the laboratory to avoid the effect of the prevailing atmospheric conditions.

The on-field experimental configuration is shown in Fig. 11 and Fig. 12, and the main components are described below:

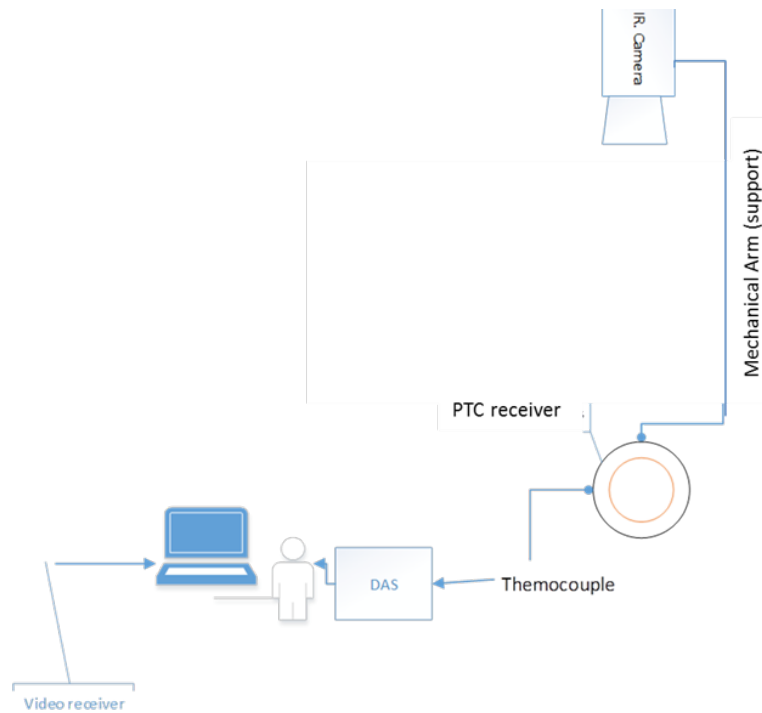


Fig. 11. Schematic view of the of field experimental setup.

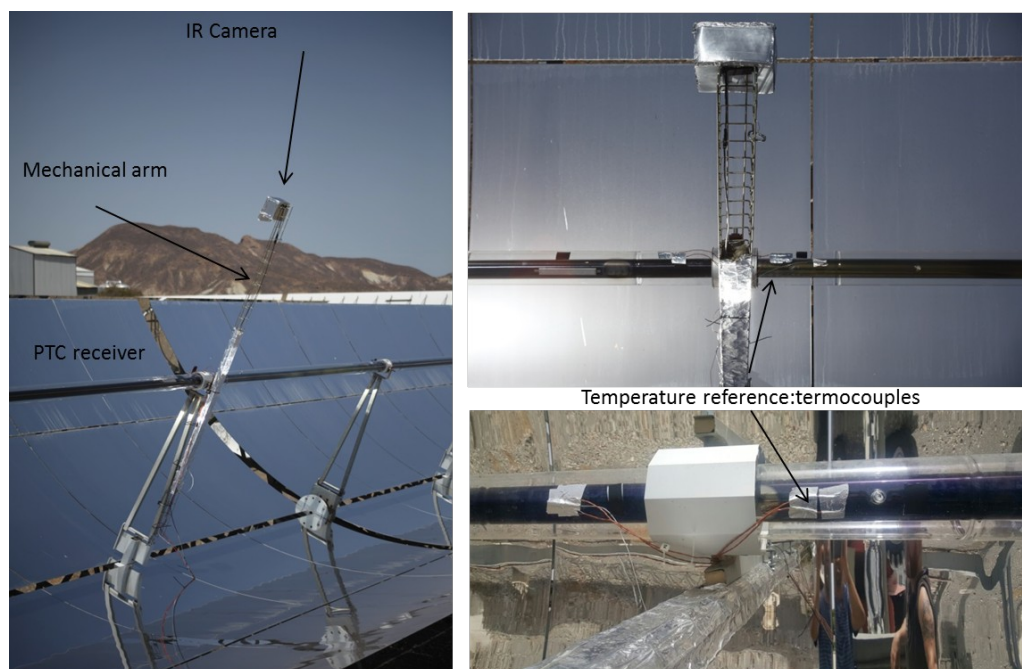


Fig. 12. Aspect of the field experimental setup.

Temperature monitoring system:

- **Contact temperature sensors:** The glass temperature was measured with 5 T-type thermocouples. Moreover the temperature of the absorber was considered equal to the HTF temperature

measured with 4 PT-100.

- **IR camera:** An IR camera (Optris Pi640) has been used. This camera has an accuracy of $\pm 2^{\circ}\text{C}$ and a temperature resolution (NETD) of 0.075°C within the $7.5\text{-}13\ \mu\text{m}$ spectral range, and it's small and light to be used in a UAV. The camera has been equipped with a super wide angle lenses ($90^{\circ}\times 66^{\circ}$). It was installed at 1.3 metres from the receiver tube on a mechanical arm to acquire images of the receiver tube from the sky. This configuration allows monitoring 3 metres of the tube at a short distance (1.3 m) with a pixel size of $5\times 4\ \text{mm}$.

Temperature obtained from IR images (T_{IR}) has been calibrated with the temperature data obtained with the thermocouples ($T_{\text{TH-field}}$). To that end, $T_{\text{TH-field}}$ has been defined as function of T_{IR} , and the calibration function is obtained as $T_{\text{IRc}} = T_{\text{TH-field}}(T_{\text{IR}})$. The calibrated T_{IR} will be named T_{IRc} .

Data acquisition system: The thermocouples signals were recorded with a portable data logger (Graphtec gl200 midi logger) and the PT-100 data were recorded with an IMP 359555 J data acquisition system. The IR camera measurement data are recorded and stored in a Lenovo L460 laptop and post analyzed with Optris Pi connects software.

3.2 Results and discussion

These measurements have been carried out in irradiated tubes and non-irradiated tubes. The main difference between both tests is that in the first case the PTC is tracking the sun and in the second case there is no sun tracking and the PTC receivers are heated indirectly by heating the thermal oil with electric coils.

Fig. 13 shows the glass temperature measured with the thermocouples ($T_{\text{TH-field}}$) and IR camera (T_{IRc}) as function of absorber temperature for a non-irradiated and irradiated tube with vacuum ($10^{-4}\ \text{mbar}$) and without vacuum ($10^3\ \text{mbar}$). Moreover for comparison purpose Fig. 13 shows the glass temperature measured in laboratory with thermocouples ($T_{\text{TH-lab}}$).

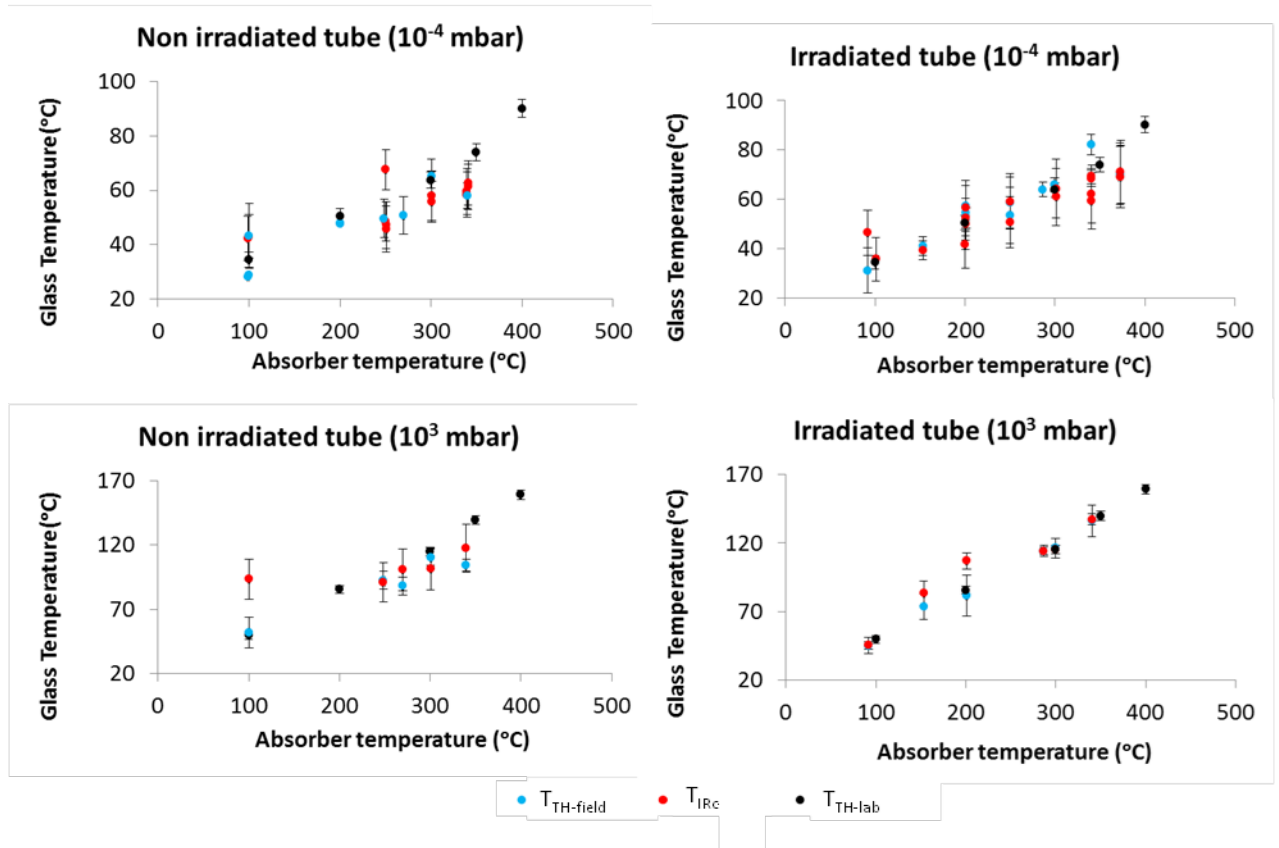


Fig. 13. Irradiated and non-irradiated PTC receiver tubes glass temperature as function of absorber temperature.

As can be seen the T_{TH} of irradiated and non-irradiated tubes match pretty well with TTH-lab. These results demonstrate that during the performed test campaign the atmospheric conditions do not have a big influence on the glass temperature. Another interesting results is that the glass temperature in irradiated tubes is not higher than in non-irradiated tubes which indicates that these measurements can be carried out during the normal operation of the plant.

In the same way that it was done with the laboratory data, the glass temperature data obtained with thermocouples have been used to calibrate the IR camera images. In order to minimize the effect of changing environment (sky temperature, wind, clouds) the IR images were calibrated with the thermocouples data obtained in the same day. Fig. 13 also show that TIRc-field is in good concordance with the temperature measured with thermocouples. However the precision is lower in the acquired measurements with the IR camera.

Therefore, it can be concluded that it's possible to apply the surface temperature method with a UAV and check the vacuum status of the tubes from the sky.

4 Check of mutual optical alignment receiver-reflector for parabolic-trough and linear-Fresnel modules

As a good rule, the answer starts with the right question. In field, in front of a parabolic-trough / linear-Fresnel module, the right question one should ask is not “how good is the facet shape?”, but “how good is the mutual optical alignment reflector-receiver?”.

About ten years ago the Visual Inspection System (VIS) method was outlined and patented [1]. The VIS approach is based on the idea of placing a source nearby the focus of the concentrator and acquiring a number of images in the near-field from different positions. On the basis of the VIS approach the following instruments have been developed:

- VISfield, to verify the mutual optical alignment between receiver tube and parabolic trough reflector for modules in field [2];
- VISshed, similar to VISfield, but permanently installed in the shed where modules are assembled, before their final location in field [3];
- VISprofile, for the shape measurement of parabolic-trough facets in laboratory/industry [4];
- VISdish, for canting and shape-measuring of solar-dishes in field [5].

All these instruments are currently marketed by MARPOSS under ENEA's license.

In the framework of the STAGE-STE EU project, ENEA studied the portability of the VIS technique on UAVs to outline a new instrument named VISfly.

4.1 VISfly theory

The optical scheme of the VISfield is shown in Fig. 14; here the Sun is only hypothetical, and it is drawn just to explain the instrument working. Briefly, the observer (the camera) in V sees the image of the receiver spread around the point P which has the same abscissa x_v of the camera. Misalignment of facet and/or receiver causes the shift of the receiver-image from P; in the case of perfect alignment and shape, the receiver image is expected to appear in x_{min} and x_{max} . On the other hand, according to the Helmholtz's theorem about the reversibility of the light path, the hypothetical solar spot made by the beam reflected in P and hitting the receiver is always viewed between $x_{s_{min}}$ and $x_{s_{max}}$. Therefore the intercept factor is simply given by the fraction of the solar-spot-image covered by the receiver-image. In the previously published papers [2,3] a numerical method for evaluating x_{min} , x_{max} , $x_{s_{min}}$ and $x_{s_{max}}$ is reported.

The map of the intercept factor is obtained by processing some hundreds of images captured at different positions along the abscissa x , in the range of the parabola aperture. The image processing also gives detailed information on how to improve the alignment of each facet (canting). At the end, the very last shape-quality check of the panels is offered by its individual intercept-factor map [2,3].

The VISshed is a powerful instrument that can be systematically used during the solar-field construction, while the cargo trailer version VISfield can be used to analyse in-situ singular modules which are resulted defective; because of the quite long measurement time (about 1 h / module) VISfield is not suitable for the exhaustive check of the whole solar field. Conversely, when a high frame-per-second camera was embarked on a UAV to overflight modules and acquire a convenient number of frames at several abscissa values from a rim to the opposite, one could benefit of the VIS approach to infer the status of the mutual optical alignment between parabolic trough reflector and receiver. The VISfly is expected to be less accurate than VISfield, but the short measurement time (less than 1 module/minute) makes it suitable for the periodical checking of large solar fields.

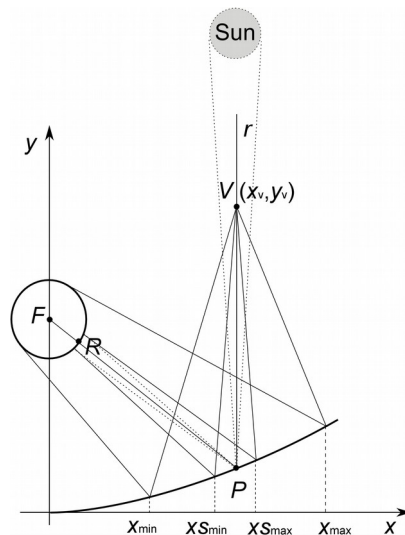


Fig. 14. Optical scheme of VISfield and VISshed.

The most serious problem for the portability of the VIS approach on UAVs is the determination of position and attitude of the camera respect to the natural reference frame of parabolic trough reflectors illustrated in Fig. 15: the X and Z axes are set to describe the ideal surface of the reflector with the parabola equation

$$z = \frac{1}{4f} x^2 \quad (\text{Equation 1})$$

where f is the focal length. The Y axis passes through the vertex loci; the frame origin is set in the middle of the module length. Ideally the receiver tube is concentric to the focus line. Please note that this reference frame rotates jointly to the module.

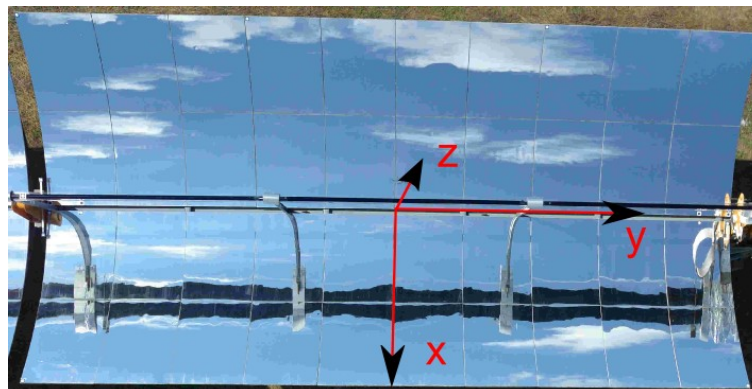


Fig. 15. Reference frame of the parabolic trough module.

Initially we saw with interest the evolutions of GPS, like Differential Global Position System (DGPS)

and Real Time Kinematic (RTK). Both are composed by two electronic devices: one has to be embarked on the UAV, while the second is must be kept on the ground in steady position. Unfortunately they are very expensive, and in the end they just allow to know the position of the drone but not the position and attitude of the camera itself, which must be installed on a gimbal to ensure a good sharpness of the taken images [6].

A much more economical solution is the apposition of a number of targets in some strategic points of the module, thus position and attitude of the camera can be evaluated by a suitable image processing based on the camera pin-hole model, which will be soon explained. Fig. 16 shows the arrangement of the adopted target set: 1&2 on the receiver tube, at the opposite sides of the modules; 3,4,5, and 6 at the four module corners; 7&10 and 8&9 are at symmetric distance from the joint-pivot axis of the module which define the rotation axis of the module. The latter couples of targets together 1&2 are essential for the correct recognition of the plane $x=0$.

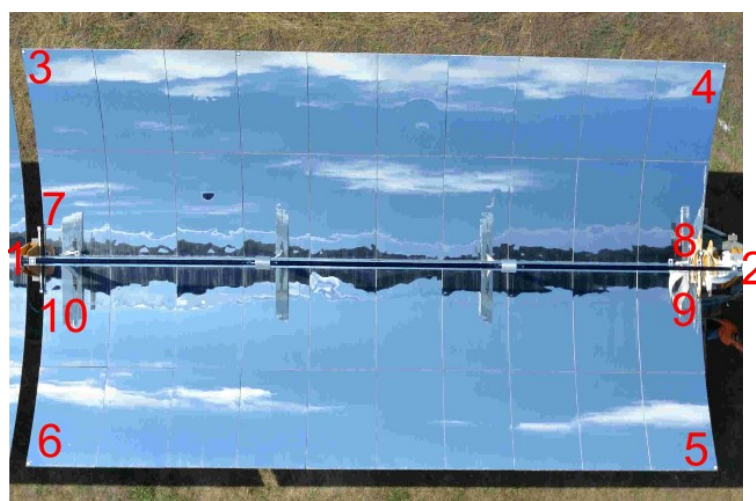


Fig. 16. Target set used to determine position and attitude of the camera on the UAV.

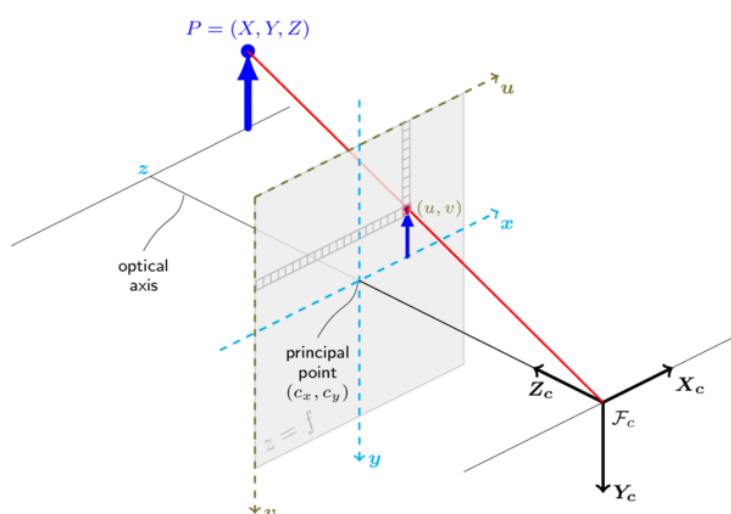


Fig. 17. Pin-hole camera model (Font: OPENCV library documentation).

The position of these targets (x,y,z coordinates) wit respect to the reference frame XYZ of the module can be obtained by conventional close range photogrammetry; at that purpose a convenient number of images must be taken from different positions. Initially we got those image from the ground, but in the future they could be selected among those of the sequence required by the VIS analysis. This last

solution is certainly much safer because modules are not perfectly rigid, thus the target position could depend on the orientation of the module. Moreover the target apposition on receiver and corners could become unnecessary thanks to their better recognizably in aerial photographs.

The pin-hole camera model is sketched in Fig. 17; it is commonly used in photogrammetry as well as in computer vision. In the figure the CCD is drawn between the object and the lens to compensate the image inversion induced by the lens, like the images provided by any modern digital camera. This model is based on a well know law of geometric optics: all para-axial rays composing the image must cross the lens in its central point. As a consequence the pixel imaging a given point P of the real word with coordinate x_c, y_c, z_c must be located along the straight line passing per P and the lens centre. Noteworthy the pinhole camera model automatically take into account the *falling lines* phenomenon occurring when the CCD plane is oblique with that of a rectangular object; that makes not necessary the adoption of any correction of the image.

The camera has an own reference frame which is completely different from the one of the module, described in Fig. 15. On the other hand these two reference frames are related one to each other by well-known equations which depend on position and attitude of the camera [7]. There are a number of different conventions about the attitude angles; the one we adopted is represented in Fig. 18. Considering the camera reference frame shown in Fig. 15, here we assume the camera is installed on the lower back of the aircraft of Fig. 18, and the UAV speed vector is along the X_c camera axis.

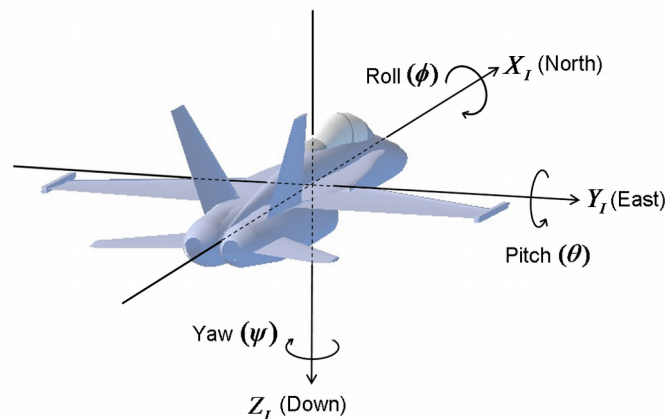


Fig. 18. Aircraft attitude angles adopted in this document.

A very important condition for the correctness of the pin-hole camera model is the use of distortion free images. As matter of fact real lens causes some distortion, more or less appreciable; moreover the principal point generally differs from the central point of the CCD as an effect of the imperfect alignment of the lens with respect to the camera body. These issues are well known in photogrammetry as well as in computer-vision/computer-graphics, where the best practices prescribes the mandatory calibration of the camera before any measurement in order to evaluate *characteristic-matrix* and *distortion coefficients*, which together allow to get undistorted images [8].

The camera calibration starts by acquiring several images of the same *scene* from different points of view and different orientation of the camera (landscape / portrait) [8,9]; the *scene* must be prepared by placing a number of targets in a volume similar to that occupied by the object one wants rebuilt its 3D shape. For optimal performances, mono-focal are preferable than zoom lenses; in any case focus should be kept in the same fixed position for calibration and measurement because otherwise distortion and principal points could be not exactly the same.

4.2 VISfly experimental

The VISfly methodology was tested with some preliminary flights conducted by the highly skilled UAVs player Nuova Sistemi Srl, which was chosen among the most important Italian operators. The ENEA choice of entrusting the flight to a third party was dictated by several reasons: i) the Italian rules about UAV are quite complex and continuously changing; ii) initial and maintenance cost of a professional UAV is several tens of thousands of Euros; iii) nowadays UAV technology sees a tumultuously development which makes rapidly obsolescent any vehicle.

The first flight was spent to outline the flight procedure for acquiring suitable images of the module for VISfly purposes. We found that before to start the scan of the module, two goals must be achieved:

1. bring the UAV over the centreline of the module;
2. approximate alignment of the camera axis to the parabola Z axis.

Two optical phenomena offered by the parabolic trough shape can be used as guidance:

- A) with good approximation, the drone image appearing on the module surface has the same y value of the UAV itself (see Fig. 19);
- B) as shown in Fig. 20, when UAV is close to the $x=0$ plane, the receiver tube is sighted with the vertex line.



Fig. 19. UAV and its image have about the same value of the y coordinate.

Once the UAV is overflying the module centre, the airborne camera has to be oriented to make parallel the row pixel with the module rims, and to centre the module in the image. After that the pilot should move the UAV along the x axis until the receiver image reaches one of the module rim, then start the image acquisition and slowly move the UAV toward the opposite rim along the X axis.

Preliminary to the flight, the coordinates of the targets shown in Fig. 16 were evaluated by conventional photogrammetry with a Nikon D800 f 24 mm and the commercial software IWitness [9]; the results are reported in Table 2. Of the two targets placed on the receiver tube, 1 and 2, only the

latter was considered to set the plane $x=0$ because the other resulted not perfectly aligned to the centre of the receiver.

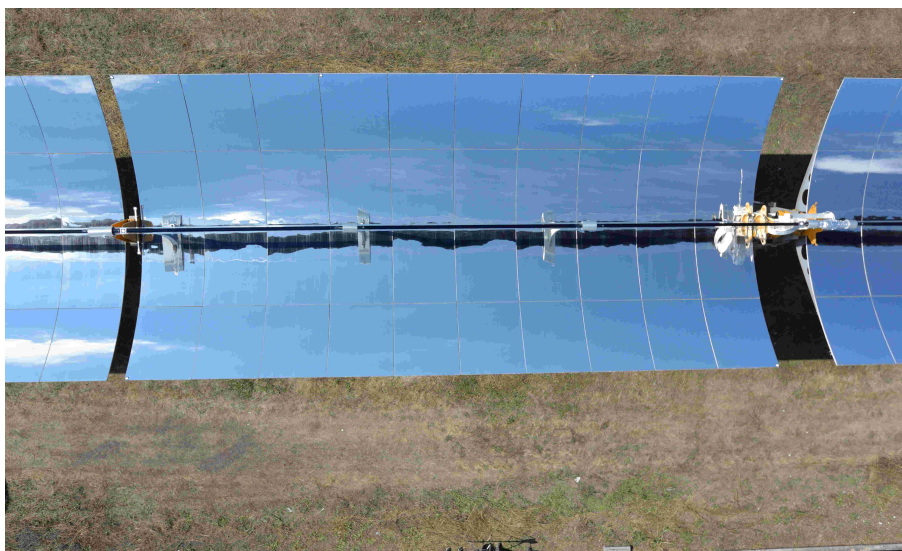


Fig. 20. At $x=0$ the receiver tube is sighted with the vertex line.

| Target No. | x (mm) | y (mm) | z (mm) |
|------------|---------|---------|--------|
| 1 | 28.5 | -5637.1 | 1875.3 |
| 2 | 0 | 6052.8 | 1868.3 |
| 3 | -2942 | -6022.4 | 1192.6 |
| 4 | -2935.9 | 6022.4 | 1190.2 |
| 5 | 2921.3 | 6010.9 | 1178.8 |
| 6 | 2931.5 | -6017.5 | 1179.9 |
| 7 | -464.7 | -6074.9 | 195.7 |
| 8 | -232.7 | 6022.1 | 89.7 |
| 9 | 232.7 | 6037.8 | 242.6 |
| 10 | 464.6 | -6070.3 | 136.4 |

Table 2 Target coordinates

For the sake of the flight autonomy, compact cameras are preferable than DSLRs. We chose a Nikon AW1 f 10 mm which also has the film shot option. Unfortunately the first lesson we learned was that the images we need must be acquired as a sequence of regular photographs: as matter of fact film frames are obtained by reading the CCD pixels along an interval of time, but meanwhile position and attitude of the UAV may change. As a consequence, film frames may be less sharp than photographs.

The VISfly methodology was tested by analysing one of the eight modules composing the PCS facility of ENEA-Casaccia by means of the hexacopter shown in Fig. 21. During the flight the collector was pointed towards the vertical. The images were processed by a custom software wrote in C++ based on the OpenCV library which offer a very rich and complete tool box for managing digital images. Each useful image was processed by the following steps:

- 1) Undistort the image by the knowledge of camera matrix and distortion coefficients (previously determined).

- 2) Evaluation of the pixel-coordinate of the centroid of each target.
- 3) Best fit of the experimental centroid set with that predicted by the pinhole camera model where UAV Position (x,y,z) and attitude (yaw, pitch, roll) are the fit parameters.
- 4) Computing of expected positions of receiver tube and solar spot according to VIS approach.
- 5) Evaluation of the intercept factor as the portion of the solar spot area covered by the real image of the receiver.



Fig. 21. Hexacopter by Nuova Sistemi Srl equipped with a Nikon AW1 compact camera.

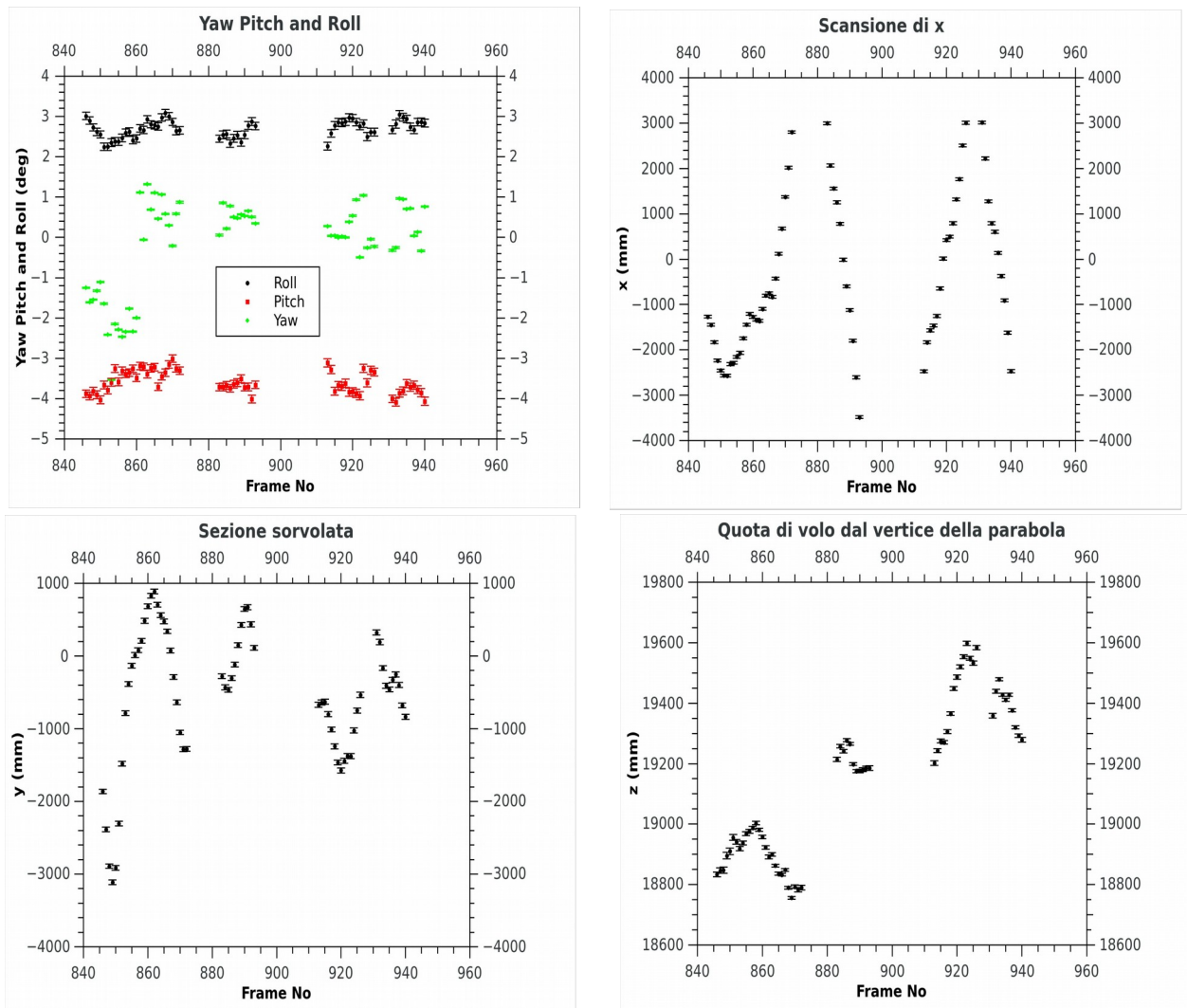


Fig. 22. Attitude (top left), x (top right), y (bottom left) and z (bottom right) of the hexacopter during the overflight of one of the PCS module.

The experimental values of attitude and position are shown in Fig. 22. Among the attitude angles, Yaw spans the largest range, between -2° and $+1^\circ$. The distance from the parabola vertex ranges between 18.7 and 19.6 m. The overflight y value ranges between -3 and +1 m; in the future the pilot should pay more attention to keep the UAV more close to the $y=0$ plane during the scan of the module.

The precision of attitude and position was evaluated by modifying each one of the target pixel coordinates for a random error and relaunching the fit procedure; this was repeated thousands of time by assuming a normal distribution with standard deviation of 0.1 pixel. The error at 3 sigma is: $\pm 0.01^\circ$ for Yaw, Pitch, Roll, ± 3 mm for x and y, and ± 7 mm for z.

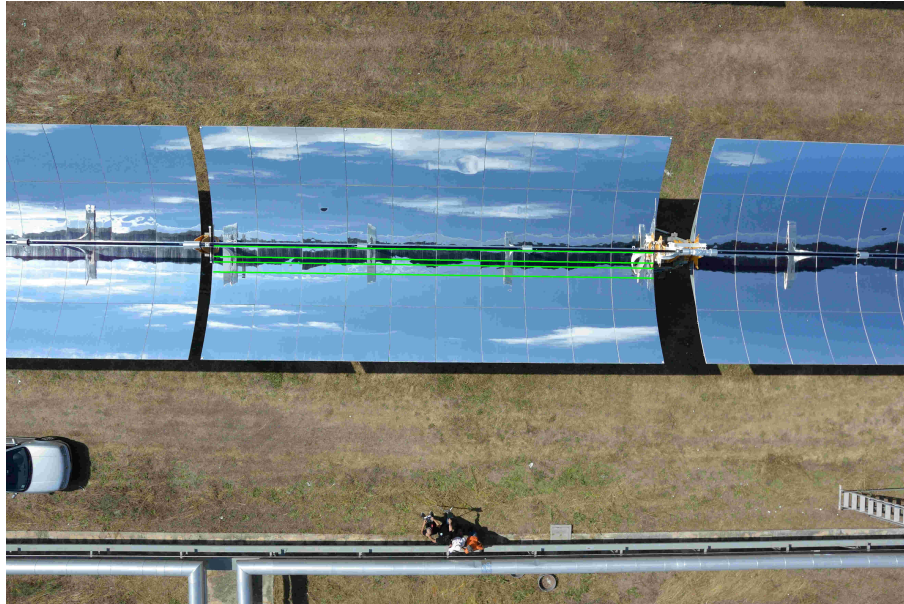


Fig. 23. Example of overlay with the expected position of the receiver image and solar spot.

Fig. 23 shows an image where the expected position of receiver and solar spot (at normal incidence on the module aperture) are drawn by green lines. The intercept factor is given by the portion of the solar spot region covered by the real image of the receiver tube.

Fig. 24 shows the behaviour of the intercept factor along the module overflowing. The low performance around $x=\pm 1600$ mm and $x=0$ mm is mainly due to the *edge effect*: because of the material discontinuity, close to the linear edges of the panel is quite difficult ensure the right shape. The reduction around $x=-1800$ mm is due to shape defects; the major is the evident swelling on the surface of the 6th panel from the left. The low intercept factor for $x > 2800$ mm is in agreement with ground measurements: the geometry of the supporting structure is a bit different among the two half part of the parabola ($x < 0$ and $x > 0$) as a consequence of a not optimal assembling; so that the slope in the the half-part $x > 0$ is a bit lower than the one of the ideal parabola. This is confirmed by the lower z values of the corner targets 5&6 respect to 3&4, for about 12 mm.

Because of the limited frame rate offered by the Nikon AW1 camera, the sampling density was not sufficient to draw the intercept factor map. To overcome this problem MARPOSS has kindly financed the purchasing of the smart camera Matrix Vision *mVB1ueLYNX-X125AG* (2448 x 2050 pixels), global shutter, 10 frame/sec. Unfortunately after the above reported preliminary flights, the PCS facility has been first busy with the EU project HITECO and after out of work for a long period to be completely renewed to the new collector version adopted in Egypt for the EU project MATS. Only from June 2017 the collector operativeness was partially restored, but in the remaining period until the end of the STAGE-STE project, the drone player has not been available for further experimentation.

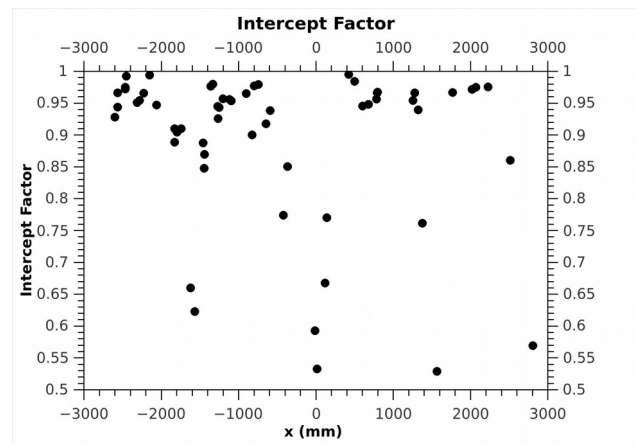


Fig. 24. intercept factor by the image processing.

4.3 VISfly conclusions

The preliminary experimental data herein reported clearly demonstrate the feasibility of the VIS methodology for aerial inspection of large solar field. In particular the experimental activity has allowed to define the following points:

1. Procedure for camera alignment and flight management.
2. Number and arrangement of the targets for the evaluation of position and attitude of the UAV.
3. Relationship between 3D point coordinates and pixel coordinate by means of the pinhole camera model together with the transformation between the two different reference frames of camera and parabolic trough module.
4. Software, wrote in C++ and based on the OpenCV library, for the image processing to obtain UAV position and attitude as well as the intercept factor according to the VIS methodology.
5. Need of a high frame-rate high resolution camera.

Although the experimental activity concerned only parabolic trough modules, it should be stressed that the VIS methodology can be easily adapted to linear Fresnel collector too. The only important difference is in the choice of the reference frame: should be set on the ground, with Z aligned to the vertical, and crossing the centre of the receiver tube; Y parallel to the receiver tube and the row of mirrors. The rest of the analysis is completely similar to that above described.

5 Flux measurement system

5.1 Description

A system to measure the flux distribution in the focal region of a Fresnel solar plant was developed and tested. The measurement is done thanks to several CPV cells fixed on a transversal bar located below the receiver. The bar is able to move along the receiver to acquire an entire flux map. The cells were calibrated under an AM1.5 spectrum. It was checked that the variations of the short circuit current between the cells used was negligible. Nevertheless, the response of the cell depends on their temperature, the direction of the incident light and on the incident spectral distribution of the light. The entire system is cooled to guarantee that all cells are at the same temperature during the test. Because we do not know exactly the direction and the spectral distribution of the light incident to the receiver, CPV cells responses are used as a relative signal. A Vatel thermogage located at a same transversal position as a particular CPV cell is used to calibrate the signal delivered by the CPV cells. The thermogage is also cooled.

The Fresnel prototype where the flux measurement system was tested is made up of a solar field of 10 lines (1 m width, 5 m long) that track the sun to focus on a receiver of 20 cm wide by 5 m long. Each CPV cell is 1 x 1 cm installed on a support of 3.5 x 3.5 cm. 10 CPV cells are used so that the flux is measured on a width of 35 cm. On the longitudinal side, the system is able to move only 4.8 m, so we are not able to measure the entire power reflected.

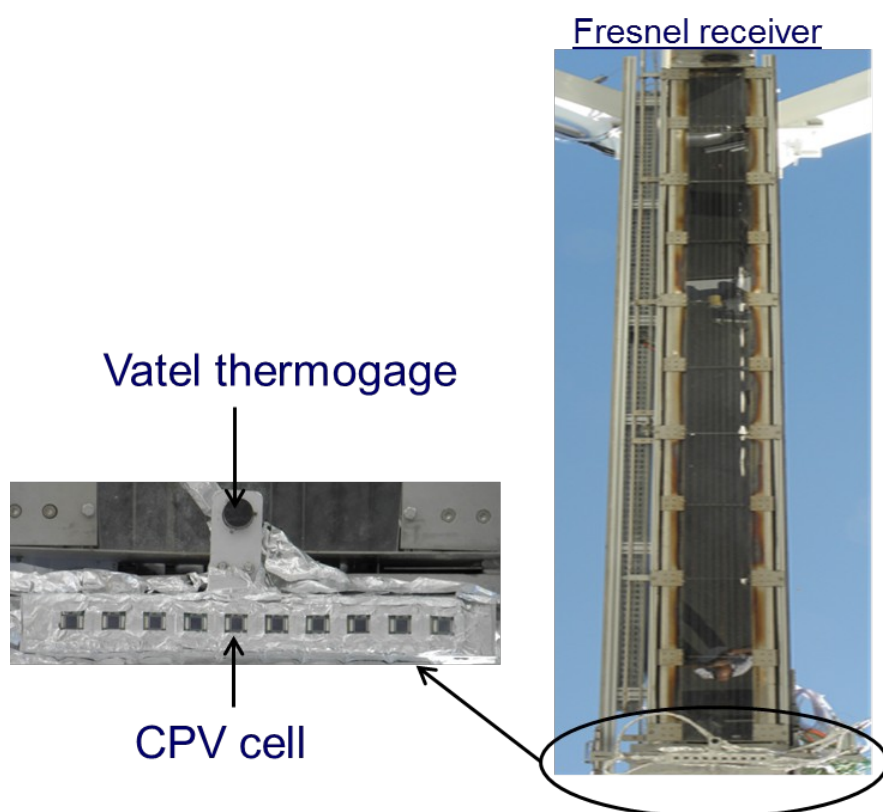
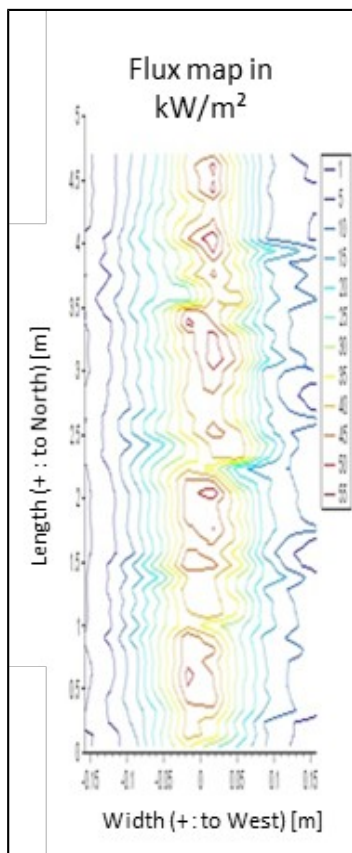


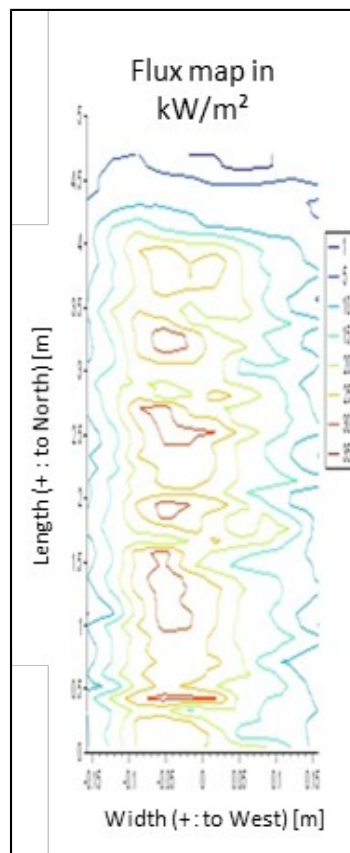
Fig. 25. Pictures of the flux measurement system

5.2 Results

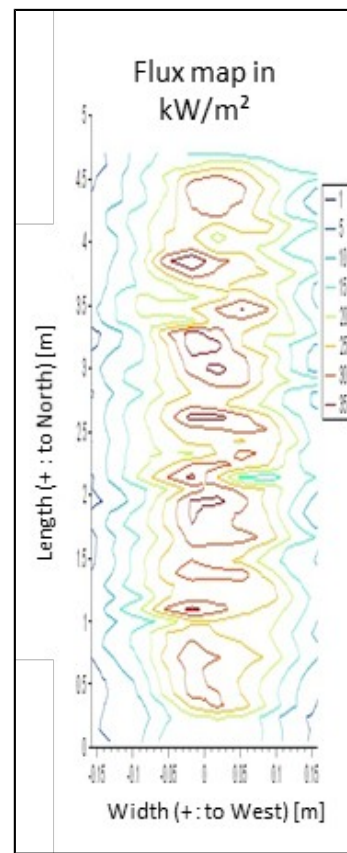
An example of results is presented below. Those 5 flux maps were measured thanks to the combination of the thermogage with the 10 CPV cells. Mean lateral profiles are also presented and the measurement is compared to a raytracing model considering a perfect optical behaviour of the solar field as well as overall optical standard deviation of 0.1° and 0.2° .



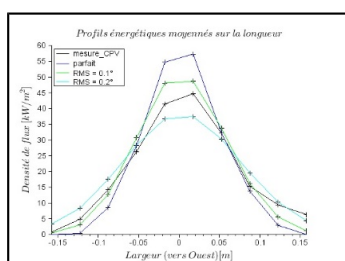
a)



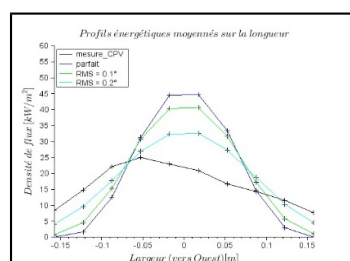
b)



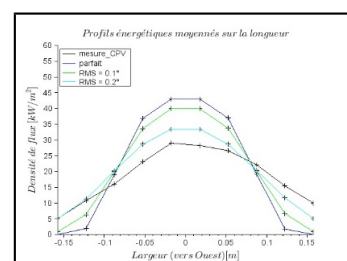
c)



f)



g)



h)

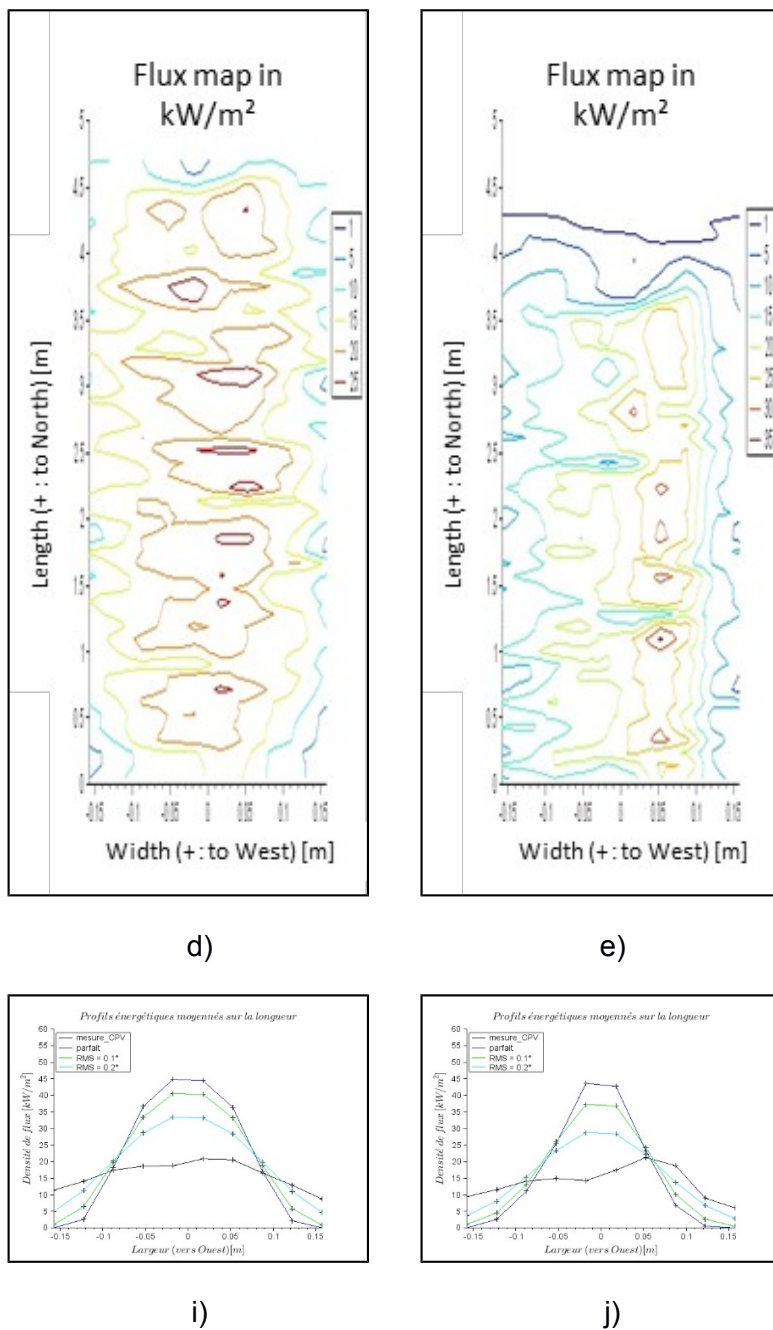


Fig. 26. Flux map measured on 01/08/15 at a) 11h13, b) 12h16, c) 13h40, d) 14h37 and e) 16h 16. Mean lateral profile at f) 11h13, g) 12h16, h) 13h40, i) 14h37 and j) 16h16

In order to check the measurement, we compare the entire power measured to the theoretical power reflected. Because the system does not measure the entire power reflected, what is not measured is estimated. We correct the measurement in that way to be able to compare it to the theory.

| | Power measured [kW] | Estimated power not measured | | Power measured corrected [kW] | Theoretical power reflected [kW] | Error [%] |
|-------|------------------------|------------------------------|----------------|----------------------------------|-------------------------------------|-----------|
| | | width [kW] | length [kW] | | | |
| 11h13 | 32.2 | 0.6 | 2.6 | 35.4 | 35.3 | 0.1% |
| 12h16 | 27.0 | 1.3 | 5.6 | 33.9 | 36.7 | -7.6% |
| 13h40 | 30.8 | 1.2 | 3.4 | 35.4 | 36.7 | -3.6% |
| 14h37 | 26.4 | 1.7 | 3.4 | 31.5 | 36.3 | -13.2% |
| 16h16 | 22.5 | 1.3 | 8.6 | 32.4 | 34.4 | -5.9% |

Table 3. Results

Except in the first case, the system underestimates the flux by about 10%.

5.3 Flux measurement system conclusion

The first trouble we meet is that the area covered by the flux measurement system is smaller than the real flux map, which does not enable us to compare the entire power measured to the theory. Besides, some uncertainties on the thermogage measurement can affect the entire flux map measured. These uncertainties comes from the fact that the direction of the incident light during the measurement is not the same as the one in the calibration done by the manufacturer. If we had known the behaviour of the thermogage according to the direction of the incoming light, some corrections would have been integrated.

At least, CPV cells measure well a relative signal. If the system measures the whole flux map, we can convert the relative signal into flux knowing the entire power we expect thanks to the theory.

Measuring the flux map enables us to deduce the optical performance of the solar field. For that purpose, a raytracing model is used and reflector shape default and tracking errors are deduced comparing measured and simulated flux maps.

References

- [1] M. Montecchi, Italian Patent RM2008A000151 (2008).
- [2] M. Montecchi, A. Benedetti, and G. Cara, Optical alignment of parabolic trough modules, <http://hdl.handle.net/10840/8591> (2010).
- [3] M. Montecchi, M. Dalla Casa, to be published in AIP proceedings of SolarPACES 2017.
- [4] M. Montecchi, A. Benedetti, and G. Cara, Fast 3d optical-profilometer for the shape-accuracy control of parabolic trough facets, <http://hdl.handle.net/10840/8592> (2011).
- [5] M. Montecchi, G. Cara, and A. Benedetti, Rev. Sci. Instrum. 88, 065107 1–7 (2017).
- [6] M. Montecchi, P. Comley, C. Villasante, F. Sallaberry, Identification of autonomous robots and UAV/IAV and completion of systems design, MS41 WP11 STAGE-STE.
- [7] H. Goldstein, Classical Mechanics (2nd ed.), Reading, MA: Addison–Wesley, ISBN 978-0-201-02918-5.
- [8] OpenCV, Camera calibration and 3d reconstruction, <http://docs.opencv.org> (2016).
- [9] iWitness Close Range Photogrammetry, <http://www.iwitnessphoto.com/iwitness/index.html>.

List of abbreviations and definitions

| | |
|-------|---|
| AIV | Autonomous Indoor Vehicle |
| CAA | Civil Aviation Authority |
| CIRCA | Climbing Inspection Robot with Compressed Air |
| CSP | Concentrated Solar Power |
| DoW | Description of Work |
| DSLR | Digital Single Lens Reflex |
| DGPS | Differential Global Position System |
| GPS | Global Positioning System |
| IAV | Intelligent Autonomous Vehicle |
| IR | Infrared |
| ITR | Inspection Receiver Tubes system |
| NDT | Non Destructive Testing |
| RTK | Real Time Kinetic |
| UAV | Unmanned Aerial Vehicle |
| UGR | Unmanned Ground Robot |
| UK | United Kingdom |
| WP | Work Package |
| VIS | Visual Inspection System methodology |